Structural and Chemical Analysis of Nanostructures by Advanced Transmission Electron Microscopy Techniques

M. Rühle

Max-Planck-Institut für Metallforschung
Seestr. 92, D-70174 Stuttgart, Germany

(Received: Jan. 30, 1997 Feb. 21, 1997)

Abstract

Nanostructured materials are materials where the length scale - in at least one dimension - ranges in the nanometer scale. The materials consists either of layered structured films (1-D nanoscale material), rod-like structures (2-D) or fine grained materials (3-D). The microstructure of the materials has to be analyzed. Firstly, it is important to identify the different phases of the material. The most adequate technique for phase identification is energy-filtered transmission electron microscopy (EFTEM). A quantitative evaluation of strains in the different constituents can be done by convergent beam electron diffraction (CBED).
Most important is, however, the analysis of the structure and composition of internal interfaces. Those defects often control the properties of the materials. In contrast to the studies of external interfaces (surfaces) there exist only a very limited number of experimental techniques for the characterization of the internal interfaces. X-ray scattering experiments and transmission electron microscopy are the most important ones.
Advanced TEM techniques will be described which can be applied for the analysis of internal interfaces. Quantitative high-resolution TEM (QHRTEM) allows the quantitative determination of the positions of columns of atoms adjacent to the interface. By analytical electron microscopy (AEM) the composition of the interfaces can be determined with high-spatial resolution and an excellent limit of detectability. From detailed electron energy-loss spectroscopy (EELS) studies information on electronic bonding, coordination number and distances to neighboring atoms can be retrieved.
In this paper the different TEM techniques will be applied to different nanostructures (ceramic composites, interfaces in metals and ceramics, and metal/ceramic interfaces.

1. Introduction

Nanostructure materials play an important role in advanced technologies. Nanostructures can be differentiated owing to the numbers of dimensions in which the length scales of the microstructure is on the level of only a few lattice parameters (nanometer scale). Therefore, one-dimensional nanostructures are thin films and layered structures, two-dimensional nanostructures are nanowires, and three-dimensional nanostructures are materials where the grain size ranges in the nanometer scale in all three dimensions. Structure and composition of internal interfaces play a crucial role for the properties of materials. Therefore, the interfaces have to be characterized in all required details.
Often nanostructures possess extraordinary properties depending on the microstructure. Therefore, it is most desirable to process and characterize a designed microstructure. For the microstructure of nanostructures several aspects are of importance. It is not only significant to process and characterize a well defined nanostructured material but also to investigate the stability of the microstructure during annealing: It is not only important to investigate the onset of grain growth but also the onset of chemical reactions which may occur at heterophase boundaries within the nanomaterials.
This paper will be organized as follows. In section 2 the different parameters which are important for a characterization of the materials will be summarized. Section 3 contains a short summary of the fundamentals of the different TEM techniques. In section 4 to 10 several techniques for the characterization of materials will be explained and their applicability for a specific nanocrystalline material demonstrated. In section 11 the results obtained for the $Cu/\alpha\text{-}Al_2O_3$ interface are described and section 12 covers the conclusions.

2. Microstructural Parameters of Nanomaterials

Table 1 summarizes the different microstructural parameters which are of interest for nanomaterials. In principle, it is possible to identify most microstructural parameters by advanced electron microscopy techniques.

Table 1 Characterization of Nanomaterials

Problem	Technique	Example	Section in paper
Identification of grain composition	ESI	Polymer-derived ceramics	5
Gradients in composition	QAEM-HSR	Interdiffusion	6
Orientation of grains	OIM, Kikuchi	Cu, polycrystal	7
Strains in materials	EF-CBED	Al films on Si	8
Composition of internal interfaces	QAEM, ELNES	$Cu(Ti)/Al_2O_3$	9
Atomic Structure of internal interfaces	QHRTEM	Cu/Al_2O_3	10

ESI Electron Spectroscopic Imaging
QAEM Quantitative Analytical Electron Microscopy
HSR High-Spatial Resolution
OIM Orientation Imaging Microscopy
EF Energy Filtering
CBED Convergent Beam Electron Diffraction
QHRTEM Quantitative High-Resolution Transmission Electron Microscopy
ELNES Energy-Loss Near Edge Structure

3. Fundamentals of Different Microscopy Techniques

In this section the different microscopy techniques are summarized. For more details the reader is referred to specific textbooks or articles (conventional transmission electron microscopy (CTEM) [1-5], high-resolution transmission electron microscopy (HRTEM) [4-9], analytical electron microscopy (AEM) [4,5,10-15], scanning tunnelling microscopy (STM) and atomic force microscopy (AFM) [16-18], scanning electron microscopy (SEM) [19-21], orientation imaging microscopy (OIM) [23-25]). Advanced materials research requires the characterization of crystalline materials to the atomic level. Transmission electron microscopy (TEM) plays a major role within the techniques which are used for materials characterization. However, studies on surfaces of materials are also often required. The latter techniques do not require a complicated specimen preparation.

3.1 Transmission Electron Microscopy Techniques

Within the last decade astonishing advances in the instrumentation in TEM have occurred. Besides CTEM, new techniques are emerging which are based on very specialized instruments. With those advanced methods dynamical processes can be investigated, atomistic structures can be studied and the chemical composition can be determined with extremely high spatial resolution. Figure 1 summarizes the different TEM techniques. Each column stands for a specialized technique in the area of microstructural characterization. An optimum application of a specific technique requires a specific instrument.

The advancements in instrumentation promote and necessitate further development in the methodology of TEM. All information included in a TEM micrograph should be evaluated and whenever possible quantitative data on physical parameters extracted. In many cases this requires extensive image processing and frequently also computer simulation to retrieve the required information content. Whereas in many fields these new quantitative techniques are only at their beginning, in the field of materials science a number of different methods for the characterization of nanocrystalline materials are already well established.

3.2 Studies of Surfaces

Scanning electron microscopy [19-22] is a standard technique for the investigations of the topography, morphology of surfaces and of the composition of surface near regions. Through the advent of scanning probe techniques [16-18] a characterization of surfaces to the atomic level is possible. It should be kept in mind that Auger investigations [22] reveal the chemical composition with high accuracy and with a spatial resolution approaching the nanometer scale (Scanning Auger Microscopes: SAM).

Recently, new techniques were developed [23-26] which allow the determination of the misorientation of different grains: orientation

imaging microscopy (OIM). In this microscopy contrast is formed by gradients of local lattice orientation. More specifically, backscattered Kikuchi patterns are analyzed to evaluate lattice orientation of small localiz regions of $\lesssim$ 100nm. This technique is most interesting for the determination of the local distribution of grain orientations within a nanostructured material.

4. Specimen Preparation for Microscopical Studies

For optical microscopy as well as scanning electron microscopy the surface of the specimen has to be prepared by polishing and etching [27,28]. Thermal etching plays an important role especially for ceramics or materials containing ceramic components. The threedimensional shape of grains and the grain size distribution can be determined by stereological techniques [29].

TEM investigations require specimens with thicknesses in the range of 10nm to 30nm. The preparation of such specimens is often an extremely difficult and time consuming task. An excellent thin TEM specimen is a prerequisite for a sucessful TEM investigation. Therefore, much, but not yet sufficient, attention has been drawn to the specimen preparation techniques [30-32], specific preparation techniques were evaluated for cross-section specimens [33,34].

5. Identification of the Chemical Composition of Grains by Electron Spectroscopic Imaging

5.1 Fundamentals

Electron spectroscopic imaging (ESI) [13,35-37] was applied for an efficient and fast characterization of the chemical composition of different grains. With ESI, images showing the distribution of various elements in large specimen areas (several μm^2) at high resolution (2-3nm) [38] can be produced within a short period of time (less than 1 minute for one element). ESI is based on the use of an imaging energy filter. ESI makes it possible to image the distribution of a certain element via the characteristic energy losses which an electron beam may suffer in inelastic scattering processes with the atoms in the sample. Hence, Energy Filtering Transmission Electron Microscopy (EFTEM) has become an important tool for the microstructural characterization of composite microstructures.

In this section studies will be focused on investigations of Si_3N_4/SiC-composites, which exhibit desirable materials properties such as thermal, chemical and oxidation resistance and thus are suitable materials for high-temperature applications. Monolithic Si_3N_4/SiC ceramics were produced by polymer pyrolysis of polysilazane precursors. In contrast to earlier studies [36], the composites were crystallized without the help of sintering additives [39]. The final grain size of the composites can be controlled by doping the starting materials with B or P. B doping leads to nanocomposites which do not contain any sintering additives, in contrast to materials produced by the traditional powder metallurgical method. The preparation of the bulk material is described elsewhere [37,39]. After annealing SiC and Si_3N_4 crystallizes out of the amorphous component.

A Zeiss EM 912 Omega TEM has been used for the investigations. This instrument represents the first commercially available EFTEM with an imaging Omega filter [40]. The design of the Omega filter is schematically shown in Fig. 2a. An imaging filter combines two properties: (i) The symmetrical arrangement of prisms transfers an image without distortions to the achromatic image plane; (ii) the energy dispersion of the whole arrangement of prisms causes the paths of electrons with different energies to separate and to form an energy loss spectrum at the exit surface of the Omega filter. In this energy dispersive exit plane, electrons within a defined energy loss interval $\Delta E_1 < \Delta E < \Delta E_2$ can be selected by inserting an energy selecting slit. Only these electrons will contribute to a magnified "ESI" image which can be produced by focusing the following lenses of the projector system to the achromatic image plane. Elemental distribution images are obtained using the three-window technique (Fig. 2b). Two ESI images are acquired in the structureless background before the edge caused by inner shell losses. From these two images the background can be extrapolated for each pixel and subtracted from the third ESI image which is acquired above the edge and contains the element-specific signal. An energy window width of 30eV was used.

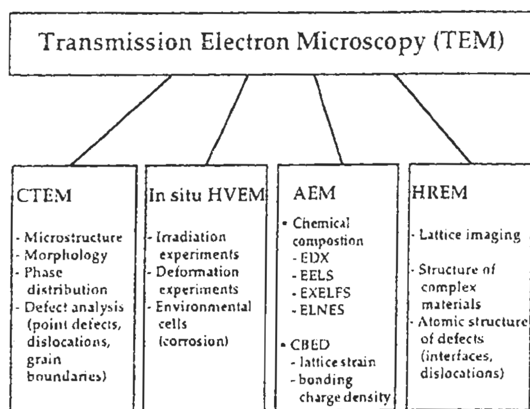

CTEM: Conventional Transmission Electron Microscopy
HVEM: High-Voltage Electron Microscopy
AEM: Analytical Electron Microscopy
HREM: High Resolution Electron Microscopy
EDS: Energy Dispersion X-Ray Spectroscopy
EELS: Electron Energy Loss Spectroscopy
EXELFS: Extended Electron Energy Loss Fine Structure
ELNES: Electron Energy Loss Near Edge Structure
CBED: Convergent Beam Electron Diffraction

Fig. 1 Different transmission electron microscopy techniques

Electron transparent specimens were obtained by mechanically sectioning the bulk specimen into 3mm discs, polishing and dimpling the 3mm discs, which was followed by a final Ar^+ ion beam thinning [33,34]. HRTEM studies were performed on a JEOL 4000 EX with a point-to-point resolution of 0.165nm [5].

5.2 Experimental Results for Polymer-Derived Si-Based Nanocomposites

The ceramic materials received after pyrolysis at 1000°C of the pure and the B- and P-doped polysilazanes were shown to be amorphous by X-ray diffraction and by diffraction studies in the TEM. Elemental distribution images reveal a homogeneous distribution of the elements Si, C, N, and B or P with a spatial resolution of 2nm. Upon annealing at elevated temperatures in nitrogen atmosphere, crystallization of the amorphous material starts by the formation of α-Si_3N_4 grains. In the quaternary system P-Si-C-N the crystallization of α-Si_3N_4 starts at 1350°C, whereas in the case of B-Si-C-N and pure Si-C-N the formation of α-Si_3N_4 is observed at 1400°C. The evolution of the microstructure of the doped materials during the transformation of the amorphous into the crystalline state was investigated by elementar mapping and selected area diffraction in the TEM. Heat treatment of the B-doped sample at 1800°C results in the formation of composites of nanocrystalline α-Si_3N_4 and SiC grains which are below 50nm in size (Fig. 3) [37]. At 1wt% B doping occasionally large Si_3N_4 grains are still formed (Fig. 3), while at a doping level of 5wt% B all the grains are nanocrystalline.

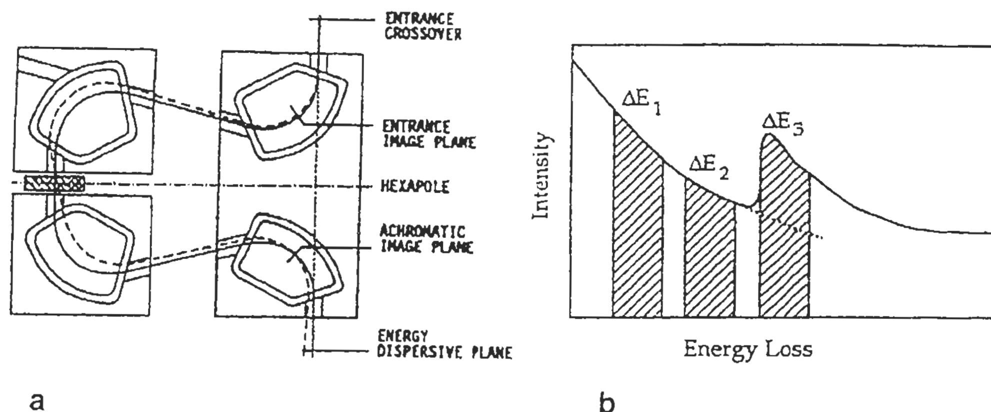

Fig. 2 (a) Schematic drawing of the Omega filter used for electron spectroscopic imaging (ESI). A slit aperture in the energy dispersive plane is used to select a particular energy loss interval. Only the contribution of the corresponding electrons to the achromatic image is projected to the viewing screen of the CCD camera below. (b) Three window technique used to produce elemental distribution images. Two ESI images are acquired in front of the edge and the extrapolated background is subtracted from the third image which contains the element-specific signal.

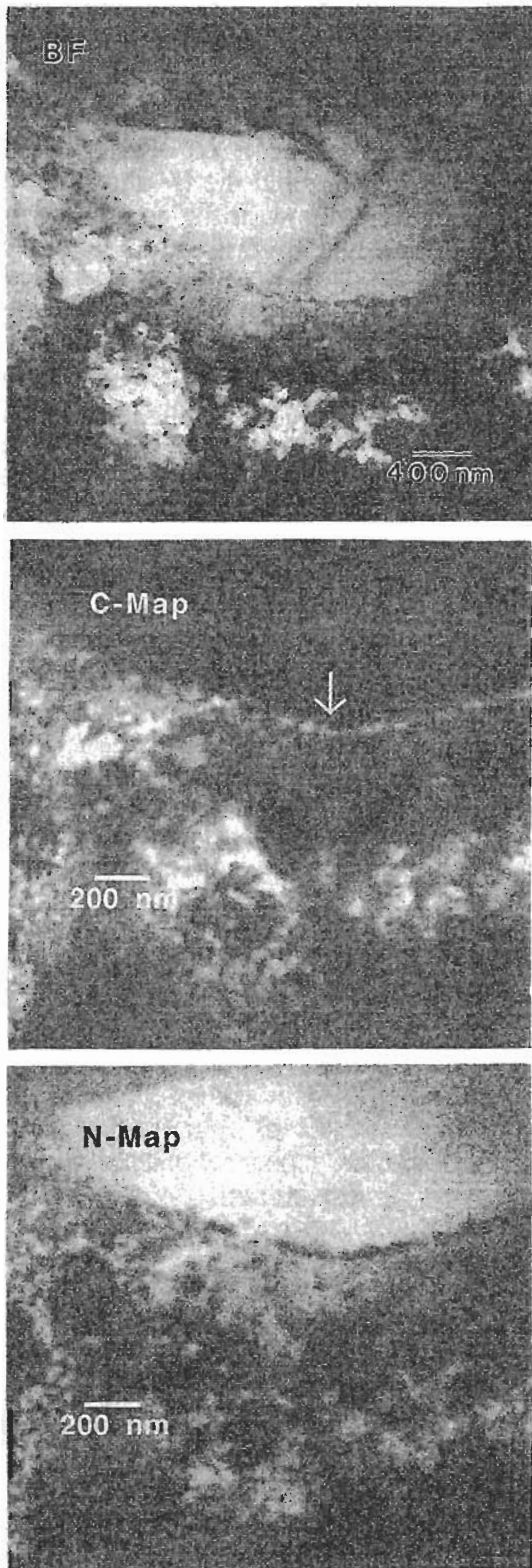

Fig. 3 Bright field image and elemental distribution images for C and N of a siliconcarbonitride material doped with 1wt% B. A few large Si_3N_4 grains are formed during the heat treatment at 1800°C. These Si_3N_4 grains are surrounded by a dense layer of SiC grains (arrowed).

B could not be detected in the elemental distribution images owing to its overall low concentration. In contrast to these results, the P-doped sample annealed at 1800°C consists of Si_3N_4 and SiC with typical grain sizes of about 0.5 - 5μm (Fig. 4) [37]. In the Si_3N_4 grains nanosized SiC inclusions are formed (Fig. 4), which is clearly revealed by the C distribution image.

The resulting microstructure of the nanocrystalline B-Si-C-N ceramic is mainly dictated by the presence of B in the material. B doping shifts the crystallization temperature of the thermodynamically stable phases to higher temperatures. B addition thus extends the existence of the single phase amorphous state

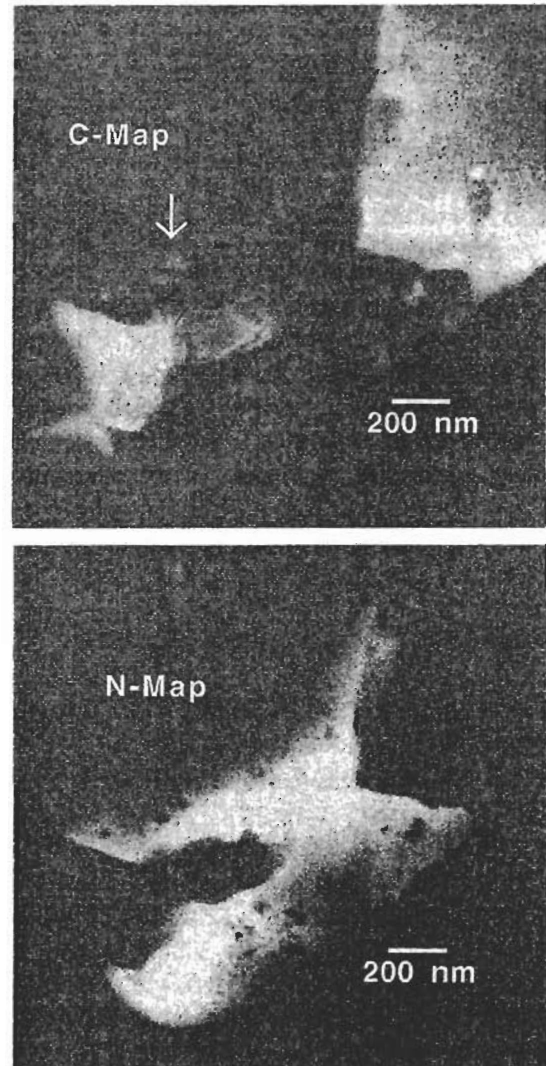

Fig. 4 Elemental distribution images for C and N of a siliconcarbonitride material doped with 1wt% P. Large Si_3N_4 and SiC grains are formed. Nanosized SiC inclusions (arrowed) can be detected in the Si_3N_4 grains, while no precipitates are formed in the SiC grains.

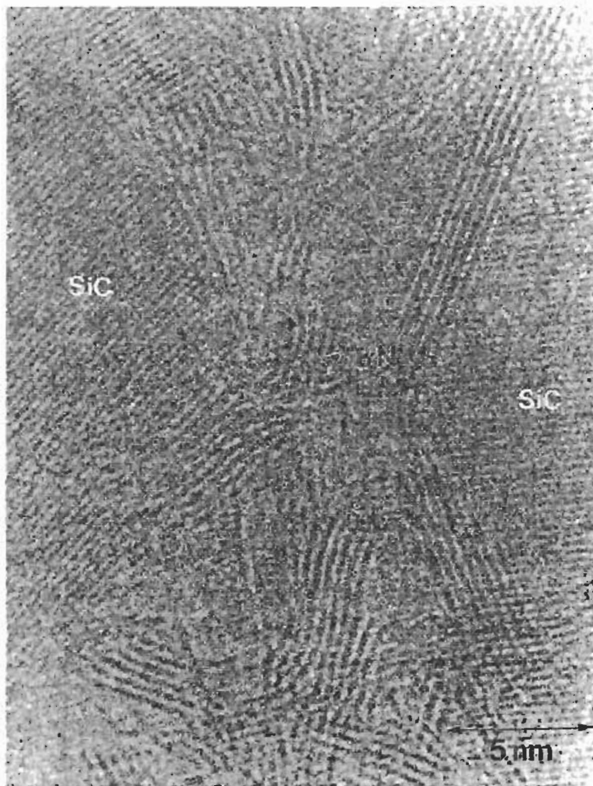

Fig. 5 HREM image showing a SiC grain coated by turbostratic BN segregations in the material doped with 5 wt% B.

to higher temperatures. During the crystallization of Si_3N_4 and SiC B diffuses out of the crystalline phases, reacts with N and forms BN which concentrates as sheet-like turbostratic segregations along the surface of the Si_3N_4 and SiC grains. The microstructure with this coating of the grains can clearly be seen on high resolution micrographs (Fig. 5). The coating results in a decrease of the mobility of the grain boundaries and the suppression of further crystal growth.

6. Determination of Variations in Chemical Composition

In nanocrystalline materials as well as in coarse grained composites chemical reactions may occur within the material, either by precipitation or between the different constituents of the material. Those reactions result in a change and/or variation of the chemical composition. Chemical reactions which occur within a material usually change the properties.

The local chemical composition can be determined on a micrometer scale by the well established microprobe technique [19-21]. The fine electron probe of an scanning electron microscope is focused on the surface of the specimen. Characteristic X-rays emit from the specimen and quantitative analysis of the X-rays results in the composition of the materials. The spatial resolution is determined by the size of the "pear-shaped" volune in which the electrons are slowed down by inelastic scattering processes. Typically the spatial resolution results in ~ 1μm [19-21].

Analytical transmission electron microscopy (AEM) allows the determination of small cylindrical regions of a thin TEM specimen. The diameter of the cylindrical region is dictated by the diameter of the probe of the electron microscope. The smallest probe size can be obtained within an instrument which uses a field emission gun as electron source. For those instruments the probe size results in ≤ 1nm. In a dedicated STEM (operated at 100kV) the probe diameter is 0.4nm [5]. The composition of the material can be determined quantitatively from signals resulting from inelastic scattering processes witin the specimen [4,5,10-12].

Over the last five years a remarkable improvement also took place in AEM owing to improved detectors [42-44]. The diode arrays in energy-loss spectrometers are noise free and all electrons can be detected. Energy dispersive X-ray spectrometers operate now digitally allowing the detection of electrons with very high density.

6.1 Studies Performed with a Dedicated Scanning Transmission Electron Microscope (STEM)

The determination of variations in chemical composition were performed with highest spatial resolution within a dedicated STEM. This allows measurements of steepest gradients. The STEM is equipped with a thin window EDS detector which allows the detection of all elements with Z > 4. A newly fitted digital pulse processor allows to obtain elemental maps within reasonable acquisition times. A parallel electron energy-loss spectrometer (GATAN 666) and a Digiscan (GATAN) are also atached to the STEM. The Digiscan allows computer control of the scanning and acquisition of digital images with this attachment concentration profiles can be determined.

In principle it is possible to obtain the analytical signals with the same spatial resolution as the image. Atomic column resolved EEL spectra have been obtained from

certain interfaces [5,45-47]. The beam current under these condition is extremely low (less than 50pA) and therefore a detector with optimum detection sensitivity is necessary. Despite the recent improvements in linear photodiode arrays (the noise component is much less) a slow scan CCD camera provides a signal-to-noise ratio which is one order of magnitude larger at these low signal intensities.
Another method for the determination of chemical variations (with emphasis on segregation at interfaces) is the so called spatial difference method [14, 48-50], see also sect.11.2. This method deliberately sacrifices some of the spatial resolution in order to facilitate the experiment and obtain reasonable signal level is. It was exclusively used for studies of segregation at interfaces. Typically a spectrum is acquired from a region $3\times4nm^2$ which contains the interface. The bulk components contributing to this spectrum are then removed by subtracting suitably scaled reference spectra obtained in bulk material near the interface. This yields the interface sensitive component of the spectrum. The advantage of the method is that beam damage is minimized and that specimen drift can easily be corrected manually.
More recently an extensive software package and some changes in the hardware have been implemented at the Max-Planck-Institut für Metallforschung [48,50]. This allows to scan the electron beam under computer control and simultaneously acquire EEL spectra. Thereby either one dimensional profiles (often sufficient for interfaces problems) [49] or full two dimensional images are obtained, where each pixel contains the full spectral information. This approach is normally called spectrum imaging, which has intrinsically the same spatial resolution as the beam diameter. The acquisition of such extensive data sets and their analysis is, however, only feasible with full computer control.

6.2 Case Study: Nb Film on Rutile TiO_2 Substrate

Thin Nb films were grown by MBE in a UHV chamber at two different temperatures (50°C and 950°C) on the (110) surface of TiO_2 (rutile) [51]. At a growth temperature of 50°C, reflection energy electron diffraction (RHEED) revealed epitaxial growth of Nb on TiO_2 with the orientation relationship (110) [100] TiO_2 || (100) [001] Nb. Auger electron spectroscopy (AES) studies revealed that a chemical reaction occurred at the initial growth state at the interface between the Nb overlayer and the substrate. A 2nm thick reaction layer at the Nb/TiO_2 interface could be identified. EELS studies revealed that an abrupt, atomically sharp transition occurs from the TiO_2 layer to the reaction layer [51].
At a substrate temperature of 950°C the Nb film was completely oxidized during growth. NbO_2 grew epitaxially on TiO_2. The structure and the chemical compositions of the overlayers have been investigated by RHEED, AES, CTEM and HRTEM [51]. With the dedicated STEM the concentration profiles could be determined across the NbO_2/TiO_2 interface for Ti, O and Nb. No "sharp" transition exists but a transition region with a width of ~44nm (Fig. 6). The concentration of O is (about) constant across the interface. In contrast, the Ti concentration drops from a constant value in the substrate (according to the chemical composition of TiO_2) to about 6at% within the NbO_2 layer. Symmetrically, the concentration of Nb increases from ~0% in TiO_2 to the maximum value in NbO_2. If one assumes that the concentration profile develops by interdiffusion then the ratio of the diffusion coefficients results in $D^{Nb}/D^{Ti} = 0.56\pm0.1$ [51]. The absolute value of the diffusion coefficient can be evaluated by including the diffusion time which is not known very accurately for the experiments done so far to ~1 h. This results in $D^{Ti}=(1.1\pm0.5)\cdot10^{-9}m^2s^{-1}$ and $D^{Nb}=(0.6\pm0.3)\cdot10^{-19}m^2s^{-1}$, respectively. The large error bars

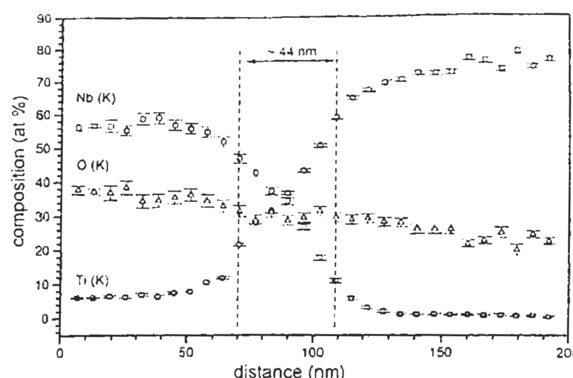

Fig. 6 Concentration profile across the interfaces between a TiO_2 substrate and a NbO_2 film grown epitaxially at a substrate temperature of 950°C. Metallic Nb was evaporated at 10-9 Torr on the substrate. No "sharp" transition exists between NbO_2 and TiO_2.A transition layer of ~ 44nm exists.

result from the uncertainty in the diffusion time.
Similar measurements were done for other systems, e.g. interdiffusion of components of a superconducting ceramic and the substrate [52] and interdiffusion at Ni/Au multilayers [53].
The concentration measurements within an AEM can be very accurate for steep concentration profiles. The technique is, so far, not applied very often. A main obstacle may be the complicated specimen preparation.

7. Determination of Local Orientation Relationship between Grains

7.1 Fundamentals

Recently, attachments to a SEM are commercially available which allow the determination of the relative misorientation between grain of a fine grained polycrystalline film (Orientation imaging mapping: OIM) [23-26]. OIM represents a sequence of mappings which reveal contrast in different colours or gray scales based upon precise knowledge of lattice orientation gradients in the polycrystal. The beam of a SEM falls into the specimen under a steep inclination angle and the backscattered electrons are detected by a sensitive CCD camera. From the position of the backscattered Kikuchi bands on the CCD camera the relative orientation between the crystal and the incoming electron beam can be determined. In the OIM the beam is stepped (in two dimensions) over the specimen (with a selected step width). From the positions of the Kikuchi bands the relative orientation not only between the direction of the incoming electron beam and specific crystallographic axes but also between different grains can be determined.
The different orientations can be colour-coded. For simple lattice structures the Σ value of the coincidence site lattice CSL [54] can be determined. The accuracy of OIM depends on the quality of the specimen surface and on the detection system and on the nature of the specimen .

7.2 Applications to Copper Interconnects

A copper film was sputtered on a glass substrate to a thickness of ~ 1μm at ambient temperatures. A SEM micrograph of the as deposited Cu film does not reveal too many details. The specimen was investigated in an OIM and the orientation relationship determined for the fine grained material. The results are shown in Fig. 7a [55]. The mean grain size is ≤ 1μm. At Fig. 7a a colour code explains the different values of misorientations. White spots mark all those areas in Fig. 7a where an overlap of grains occurs.
Annealing at 400°C results in the expected grain growth. A wide grain size distribution exists (between 0.5μm and 20μm). A texture develops as can be readily revealed from Fig. 7b [55].

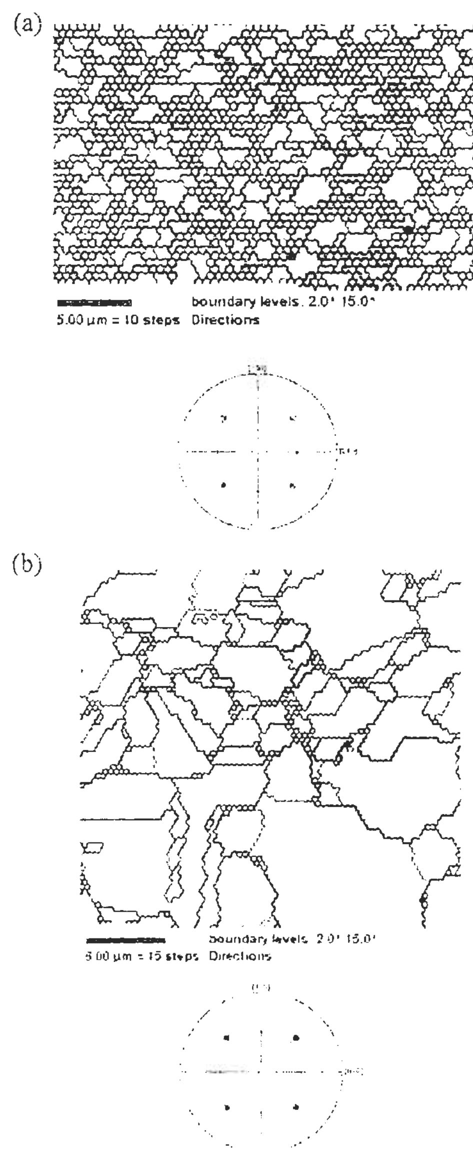

Fig. 7 Orientation imaging microscope (OIM) image of a 1μm thick Cu film on a Si wafer. (a) as deposited at ambient substrate temperature; (b) annealed at 400°C for 1h. Grain growth occurs. The colour code in the figure marks the misorientation (J. Greiser, unpublished work).

8. Measurements of Strains in Materials by TEM Techniques

Strains in materials can be determined by X-ray and convergent beam electron diffraction (CBED). The knowledge of strains (stresses) present in materials is often essential for specific material, especially for thin films used in information technologies. The strains can be caused by the difference in the thermal expansion coefficient of different materials components [56]. Large internal strains (stresses) may even cause failure. Thermally induced stresses in polycrystalline alumina scales formed as oxidation products on metallic alloys govern the adhesion properties of those scales on the metallic matrix. In this chapter measurements of thermally-induced strains in polycrystalline Al thin films on Si using convergent beam electron diffraction will be reported [57].

8.1 Fundamentals

Thermally induced stresses in polycrystalline Al thin films on Si have been extensively studied using techniques such as wafer curvature and X-ray diffraction [58]. However, these are large area methods and yield results that are averaged over the sample, rather than the local values which may be important for hillocking, electromigration-induced voiding, or stress relaxation by grain boundary diffusion. Convergent beam transmission electron diffraction (CBED) offers the possibility of achieving much greater spatial resolution compared to conventional techniques used to measure strains and stresses, because of the ability to focus an electron probe to very small size. Despite this promise of improved spatial resolution, the usefulness of transmission electron diffraction for strain determination has been limited because electrons are very strongly scattered. This leads to an effective failure of Bragg's law due to dynamical diffraction effects, and to a large inelastic background in the diffraction pattern that sharply reduces the signal to noise ratio for samples of reasonable thickness.

Recently, it has been proven possible to address these limitations and measure lattice parameters with very high precision and very high spatial resolution in the TEM by measuring the position of higher order Laue zone (HOLZ) lines in CBED patterns, and matching these positions to appropriate computer simulations which include corrections for dynamical diffraction effects [8,35,57]. ESI allows one to remove most of the inelastic background from the patterns and to more easily quantify the intensity and position of diffraction features (see sect. 5.1).

8.2 Local Strains in Al films deposited onto Oxidized Si Wafer

[111] fiber-textured Al films were grown on oxidized Si wafers to a thickness of approximately 0.22μm by UHV evaporation at room temperature. Tensile strains were induced in the Al by cycling the samples to T=450°C for 20 minutes in forming gas. This is expected to generate an equibiaxial stress of approximately +250 MPa in the Al film at room temperature immediately after annealing.

Specimens for TEM were prepared by cutting 3 mm disks from the wafers with an ultrasonic core drill. The disks were thinned from the backside to a thickness of 100μm, subsequently, the samples were dimpled to a thickness of approximately 5μm and then a window was chemically etched in the Si substrate in the dimpled region, creating a large, uniform-thickness area of Al thin film for examination in the TEM.

CBED patterns were collected on a Zeiss EM 912 Omega TEM (see sect. 3) [35]. In order to reduce contamination, the specimens were cooled during observation to temperatures ranging from –50°C to –149°C. Electrons suffering thermal diffuse scattering have energy losses too small to be removed by the filter; therefore cooling also improved the visibility of the HOLZ lines even in filtered patterns.

The Al <233> zone axis (10.02° from [111]), was chosen as having the best combination of number and contrast of HOLZ lines, proximity to the surface normal, and minimum dynamicity. Measurements were performed on grains of various sizes at this zone axis. The average grain size of Al was in the order of 0.5μm. Some abnormally large grains can easily be identified. The HOLZ line arrangement near the center of the (000) disk for a 1μm grain at T = –50°C and a 2μm grain at T = –50°C and T = –150°C are shown in Figs. 8a-c, respectively. The lattice parameters giving the best fit to Fig. 8c were used to calculate the full dynamical simulation shown in Fig. 8d. Movements of the HOLZ lines are visible both between the two grains at the same temperature and with temperature for the same grain.

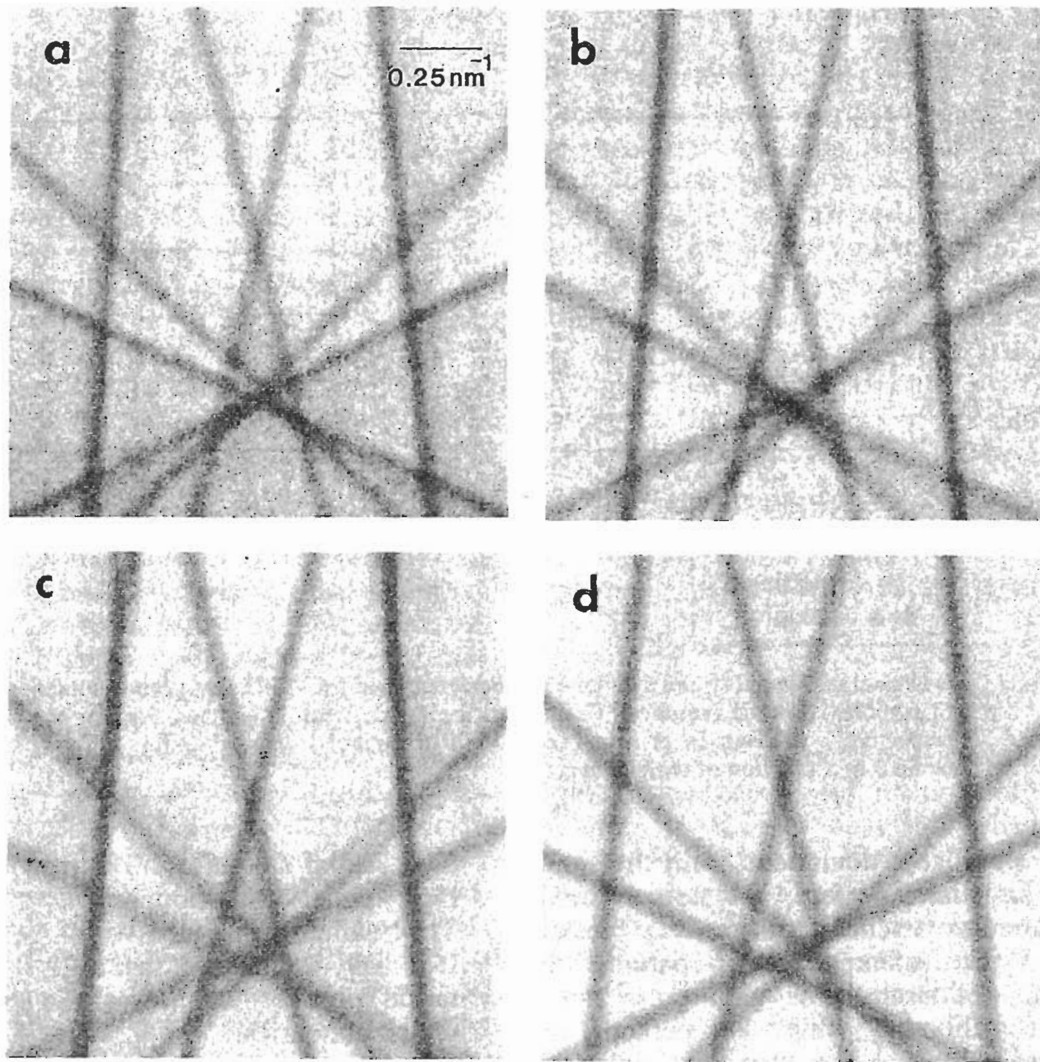

Fig. 8 [233] zone axis HOLZ line arrangements near the center of the (000) disk for (a) grain size 1 μm, T = –50°C; (b) grain size 2μm, T = –50°C; and (c) grain size, t = –150°C; (d) dynamical simulation using best-fit lattice parameters for (c).

If perfect [111] texture and equibiaxial strain are assumed in the film, the expected lattice distortions in the Al are satisfied by a trigonal unit cell given by $a_{cubic} \Rightarrow a_{trigonal}$ and $\alpha_{cubic}=90°$ $\Rightarrow \alpha_{trigonal} \neq 90°$. The [233] zone axis of such a unit cell still displays mirror symmetry, which is clearly not the case for the patterns presented here, nor for any other [233] pattern observed for these films. Reasons for this deviation from mirror symmetry include tilt of the [111] direction from the grain surface normal, dislocation effects on the strain field, and inhomogeneities in the sample, as well as any other nonequibiaxial strain and nonplane stress sources.

Although deviations from perfect [111] texture are certainly present, the deviations are generally small (<10°). Misorientations of such a magnitude are insufficient to generate the observed deviations from mirror symmetry. Therefore, the lattice parameters were refined according to a model of biaxial (but not equibiaxial) strain, using the bulk Al lattice parameters at the appropriate temperature as reference. The data for four different grains at T=–50°C, and for one grain at various temperatures, are shown in Fig. 9a and 9b. The principal strains deduced from the biaxial model (shown as filled symbols) are compared to the best fits for an equibiaxial model (squares) in these two graphs. The nonequal, biaxial model typically improved the goodness of fit, as measured by χ^2, by approximately two to four over the equibiaxial case, and by several times the measurement error.

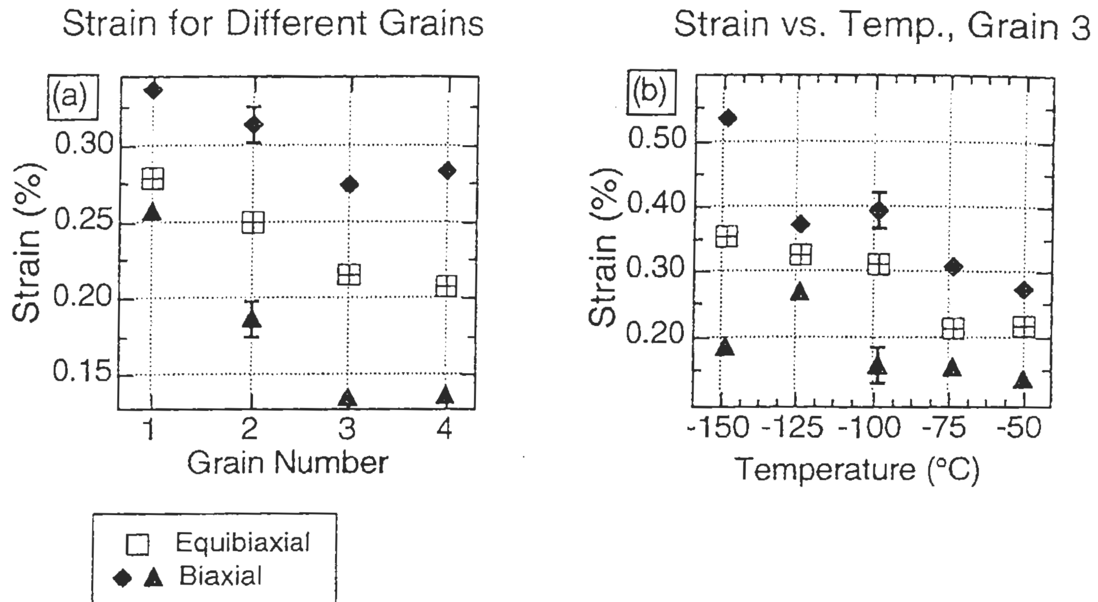

Fig. 9 (a) Principal biaxial (filled symbols) strains determined for 4 different grains, compared to best-fit equibiaxial strain (squares). Grain sizes are 1 μm, 1 μm, 2 μm and 0.5 μm, for Grain 1-4, respectively. (b) Best-fit principal biaxial (filled symbols) or equibiaxial (squares) strains for Grain 3 as a function of temperature.

Clearly, significant deviations from the simple equibiaxial strain, perfect [111] texture model are required to produce the symmetry breaking observed in the experimental patterns. No correlation of strain state with grain size is apparent, although this is perhaps not unexpected given the small number of measurements presented and the variations in the environment (exact orientation, orientation of neighboring grains, etc.) of each grain. Finally, no absolute calibration of the unstrained lattice parameter in the Al film was available, so the absolute values of the strains presented in Fig. 9 are somewhat uncertain. The relative changes for the different measurements, however, are expected to be very reliable.

9. Composition of Internal Interfaces

It is extremely difficult to measure the chemical composition at, and close to, an intact internal interface. Of course, Auger electron spectroscopy (AES) yields extremely valuable results at fractured interfaces [22]. However, it is not easy to assign the segregated species to a specific interface area. Auger spectroscopy averages the composition of segregated elements over large fractions of the interface. It is, therefore, desirable to perform measurements also at intact specimens with high spatial resolution. This can be done with high spatial resolution only with AEM in an TEM which is operated with a very fine probe. It is well established that EELS and EDS are useful tools for the study of the composition of grain boundaries.

9.1 Fundamentals

For determining the quantitative chemical composition of the specimen with high spatial resolution, both EELS and EDS can be used. The relative merits have been discussed in detail elsewhere [60]. Briefly, EDS is more suitable for heavy elements ($Z > 20$) whereas EELS is the method of choice for light elements. A typical example of an EEL spectrum is shown in Fig. 10. In the sampled volume the detection limit is typically below 1at% of an impurity element. This might not seem very good, because there are several methods which can find impurities at the ppm level [19-22]. However, those methods average over large volumes whereas the STEM is aimed at high spatial resolution. The sampled volumes can be very small, of the order of a few ten nm^3 (1nm beam diameter and 30nm specimen thickness are typical). Such a volume only contains a few hundred to thousand atoms. 1at% of that yields then a few atoms. In fact a

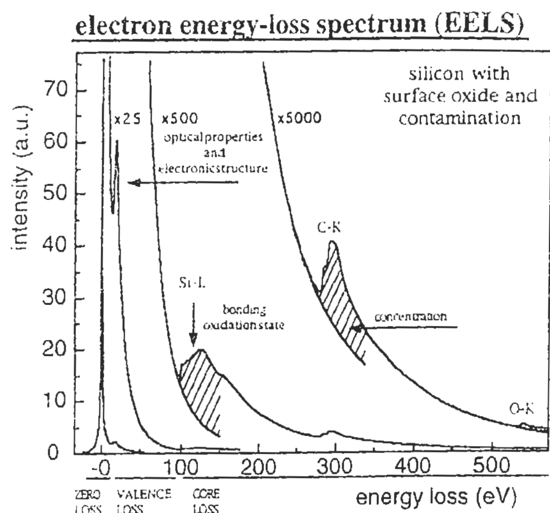

Fig. 10 Typical EEL spectrum outlining the different energy intervals. The example was acquired for Si.

single atom has been detected [61]. For applications in materials science it is of large interest to specify the composition of an internal interface. Considering the geometry a segregation of typically 1 atom per nm^2 interfacial area can be detected [62,63]. While this is the thermodynamically relevant unit, it is easier to consider the equivalent number of monolayers (ML). This value will depend on the exact definition of one monolayer, but a typical detection limit is 0.1 ML. In favourable cases it can be one order of magnitude better and even in worst case scenarios a full ML of impurity segregation will be detected.

While EDS might appear easier, it suffers from a number of drawbacks. Exact quantification is much more difficult than for EELS. Beam broadening in the specimen degrades the ultimate spatial resolution. Most important is its limitation to only determine chemical composition. EELS on the other hand contains a wealth of extra information. Since the energy resolution in an EELS spectrum is well below 1 eV, a number of spectral fine structures can be observed. Each absorption edge arising from an inner shell has superimposed on it two types of fine structure. The energy-loss near edge structure (ELNES) dominates from the edge onset up to about 30eV, whereas the extended energy-loss fine structure (EXELFS) is responsible for intensity modulations from there on up to several hundred eV above the edge onset [11,12].

One can view the excited electron as a wave which is scattered in the crystal at neighbouring atoms. The interference at the location of the excited atom decides the intensity measured in a spectrum. The mean free path for the excited electrons within the solid are short. For EXELFS this means that only paths with single

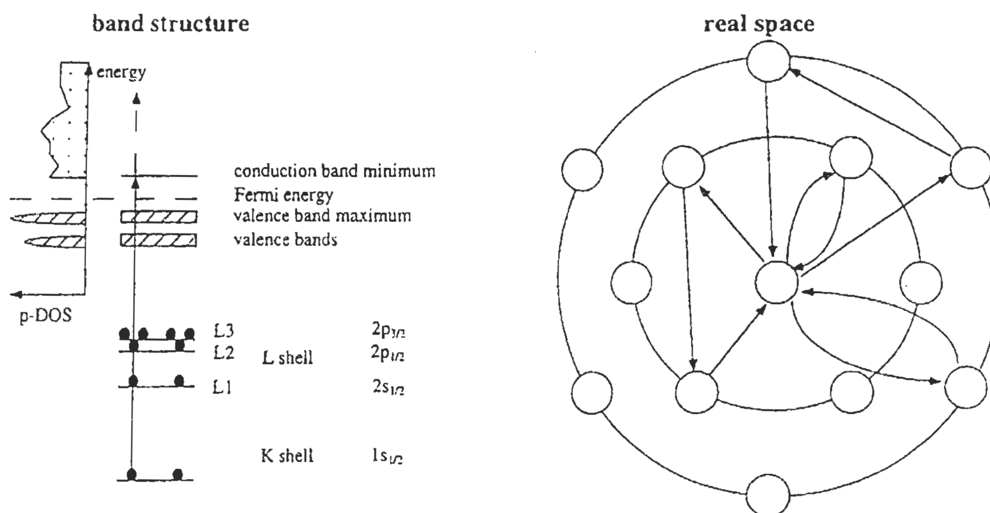

Fig. 11 Explanation of the fine structure of energy loss edges. The electron is excited from an inner shell into an unoccupied state above the Fermi level. The spectrum fine structure (ELNES and EXELFS) can be understood in terms of the electronic band structure and the unoccupied density of states. A picture in real space uses the scattering of the excited electron of its neighbours and the interference. Both pictures are equivalent for large clusters. For details see text.

scattering events have to be considered. The measured spectrum can be analyzed and yields the radial distribution function. However, this method is not used very often in the electron microscope because the achievable signal-to-noise ratio is not sufficient. For ELNES the mean free path becomes longer, so that multiple scattering has to be considered (Fig. 11). ELNES is therefore complex and cannot be analyzed directly. From this picture it is clear that the ELNES depends on coordination number, bond distances and bond angles. Multiple Scattering calculations for clusters yield the expected ELNES for a given arrangement of atoms. This approach is amenable to interfaces [64], where the more traditional band structure calculations are unfeasible, because the low symmetry requires large supercells, which are in most cases beyond the current scope of computing power. ELNES can also be viewed as transitions from occupied inner shell levels into unoccupied states in the conduction band (Fig. 11). In this view the transition rate and therefore the measured spectrum is proportional to the unoccupied density of states (DOS) in the conduction band. Selection rules apply, because under typical experimental conditions only dipole transitions are allowed. K-shell excitations probe the p-unoccupied DOS, whereas L-shells are a sum of s- and d-DOS. Furthermore the local DOS has to be considered because of the high localization of the initial state.
Changes in the ELNES are observed for different oxidation states (chemical shifts, white line intensities) and coordination [50]. The first is a more atomic effect whereas the latter depends on the environment of the probed atom. The ELNES can be used to determine the bonding, electronic structure and real space structure. The interpretation makes use of reference spectra which for some classes of material can be used as fingerprints, i.e. specific structures in the ELNES correspond to specific structural units. A more complex way of interpretation compares ELNES calculated for model structures with experimental data. This yields valuable insight into the correspondence of spectral features and real space structures. The important point about ELNES is that it contains information about the three dimensional atomic arrangement and therefore complements the information obtained from imaging, which is limited to two dimensional projections.
In the lower energy-loss region from 0 to about 50eV interband transitions and plasmon excitations occur. From such spectra the complex dielectric function of the material can be deduced. All other optical properties of the material can then be determined. The interband transition strength (which is proportional to the joint density of states including selection rules) contains information about the electronic structure of valence and conduction band [65].

9.2 Detection of a Monoatomic Layer of Ti at the Cu/Al_2O_3 Interface

Small amounts of Ti improve the adhesion of Cu to Al_2O_3 remarkably [66]. Therefore, fundamental studies were performed for a better understanding of this phenomena. Substrates of α-Al_2O_3 (with the surface plane parallel to a (0001) basal plane were sputtercleaned (sect. 11). Then Ti layers of various thicknesses were evaporated [66,67] in an MBE operated in UHV. Subsequently, a Cu overlayer of ~ 1μm was deposited. In this paper results are reported for the Cu/Al_2O_3 interface with an intermediate layer of Ti with a nominal thickness of 1 nm.
Cross-sectional specimens were prepared and then investigated by HRTEM, ESI (sect. 5) and AEM (sect. 9.1). A conventional TEM micrograph did not reveal any features indicating the presence of Ti at the interface; similarly HRTEM studies did also not allow the identification of Ti at the interface.

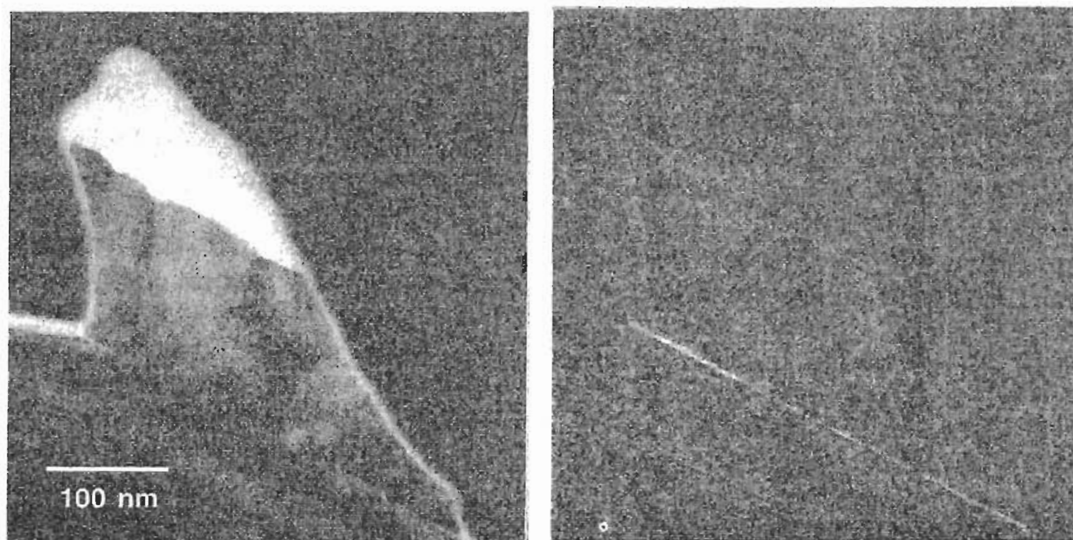

Fig. 12 Ti segregation at Cu/α-Al_2O_3 interface. Nominally 1 monolayer of Ti was evaporated on the α-Al_2O_3 substrate prior to the deposition of Cu. (a) Micrograph formed with electrons which underwent plasmon losses. The bright line at the interface indicates the presence of segregated atoms. (b) Micrograph formed with the L23-edge of Ti. The micrograph indicates that Ti is present at the interface and that the Ti distribution is not homogeneous. A quantification of the data is complicated (J. Plitzko and J. Mayer, unpublished data).

ESI (sect. 5) allows a qualitative and semiquantitative detection of Ti. Fig. 12a shows a micrograph which was taken with electrons which underwent a plasmon loss of 40 eV [68]. The light contrast at the interface demonstrates the presence of an element different from those of the adjacent crystalline parts (Cu, Al, O). An elemental mapping image taken at the Ti L23 edge is shown in Fig. 12b [69]. Light contrast at the interface demonstrates the presence of Ti at the Cu/α-Al_2O_3 interface. The different signal intensities at different interface regions suggests that the Ti is not distributed homogeneously at the interface. A semiquantitative evaluation suggests that a variation of the Ti content by a factor of 3 along the interface is possible.

The same area of the interface was investigated in a dedicated STEM. The specimen was tilted until the interface lied parallel to the incoming electron beam. The electron probe (diameter 0.4nm) was stepped perpendicular to the interface with stepwidth of 0.1nm and the X-rays analyzed by the EDS systems (Fig. 13). An abrupt change from Cu to Al_2O_3 is determined, the profile changes within a width of only 0.2nm from 0 to the value of the bulk. Ti can readily be detected at the interface. A quantitative evaluation reveals that the amount of Ti results in (0.5±0.1) monolayers [69].

From the semiquantitative observation of Fig. 12b it was concluded that the Ti concentration varies by a factor of 3 along the interface. At present time it is not clear at which area of the interface the measurements of Fig. 13 were made - in regions of high or low Ti concentrations.

ESI studies give only semiquantitative results.

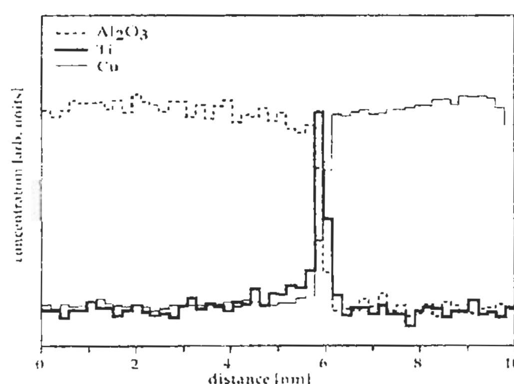

Fig. 13 Line scan perpendicular to interfaces between Cu and Al_2O_3. Nominally 1 monolayer of Ti was deposited on the α-Al_2O_3 prior to the evaporation of Cu. The electron beam of a dedicated STEM was stepped with a step width of 0.1nm across the interface and the EDS spectra was recorded. The histograms show that an abrupt change occurs from α-Al_2O_3 to Cu and that Ti is segregated at the interface. A quantitative evaluation reveals that 0.5±0.1 monolayers of Ti segregated at the interface at the investigated area of the interface.

Those observations are essential for getting an overview of the elemental distribution.
Detailed studies have to be performed with a dedicated STEM. Future studies at identical interface segments by ESI and STEM will resolve the open questions.

10. Atomic Structure of Internal Interfaces

10.1 Fundamentals and Instrumentation

To resolve the internal structure of materials at the level of interatomic spacings high-resolution transmission electron microscopy (HRTEM) was employed [4-7]. According to the theory of Abbe, resolving interatomic spacings of a crystal requires to form interference images including the transmitted wave and (at least) the first order diffracted beams. In practice one prefers to tilt the object such that the viewing direction corresponds to a low-indexed zone axis. Given that the microscope provides sufficient resolution, the interference image then shows a superposition of several sets of interference fringes. For objects of simple crystal structure one may interpret these images in terms of projected atom positions.
Interference images of sufficient contrast require special HRTEM instruments, which provide sufficient mechanical and electrical stability, highly coherent illumination of the object, and an electron optics with relatively small lens aberrations. Presently, there exist two families of HRTEMs, one with an acceleration voltage of 300kV and 400kV. These instruments possess a point-to-point resolution of ~ 0.15nm. Information for smaller distances can be retrieved by special techniques such as focus variation techniques [71] and holography [71,72] if a very coherent illumination system is applied (field electron gun). High voltage electron microscopes of the newest generation which possess a point-to-point resolution of ~ 0.1Å. High-voltage instruments are successfully applied for studying the atomic structure of interfaces [73].
Regardless of the point resolution limit the image may exhibit even smaller spacings, which must not be interpreted, however, in terms of 'projected structure'. The minimum spacing that one can observe in HRTEM images is referred to as 'information resolution limit'. The instruments with an acceleration voltage of 300 to 400kV possess an information resolution limit of 0.13nm for LaB_6 cathodes, the information resolution limit can be < 0.1nm for field emission instruments. For a high-voltage electron microscope the information limit is at ~ 0.08nm [73].

10.2 Interpretation of HRTEM Images by Digital Image Recording and Image Processing

A direct interpretation of HRTEM images of crystal defects with respect to the atomic structure is restricted to rare cases, such as thin specimens, imaging conditions free of phase reversals, or low strain fields. In practice, dynamic electron diffraction and aberrations of the electron optics lead to a complex relationship between the image and the structure of the object. For example, in the region of a crystal defect the image patterns representing projected atom columns may appear displaced against the true positions. To interpret HRTEM images 'safely', therefore, one compares them with simulated images of model structures. Frequently, the software package EMS is employed to perform such calculations [74]. While formerly it was common practice to compare experimental and simulated images by visual inspection, we have now developed procedures to evaluate image intensities *quantitatively*, by means of digital image processing [73,75].
A valid structure retrieval under dynamical electron diffraction and non-linear image conditions requires detailed numerical image simulation and image matching to the experimental image. Correspondingly, the microscopy equipment must be extended by devices for digital image recording or off-line digitization of negatives. For the processing of the digital images powerful computer hardware and software is required to handle large data fields on disk and in memory and to run time-consuming programs for off-line image restoration, structure model generation and image simulation.
Software was developed in the field of structure retrieval belongs to the fields of: (i) noise suppression at interface regions without structural distortions [76], (ii) strain field mapping at smooth interfaces [77], (iii) iterative digital image matching between simulation and experiment for automatic refinement of interface models in complex systems [78-81]; (iv) pattern location and misfit analysis at grain boundaries and phase boundaries [82], and (v) focus series reconstruction to correct the imaging aberration

for perfect crystal areas [83].

As a result of this applied image processing, quantitative numbers for structural parameters (e.g. volume expansions at interfaces) or even individual atomic coordinates at interfaces or dislocations can be given. The software also provides confidence intervals for the retrieved crystal structure coordinates, adapted to actual situation with respect to the specimen or image quality. Currently, the precision of atom location varies from 0.01 to 0.04nm depending on the elemental composition, crystal structure and projected atomic distances. Also details of the specimen preparation process, amorphous layers on the specimen or misalignment of the specimen and microscope have a big influence of the attainable precision.

It is aimed to provide this precision throughout in future which would match the requirements of comparing the experimentally retrieved structures to subtle details from theoretical atomistic simulations.

The actual list of successful (partial or full) structure retrieval by off-line image processing includes grain-boundaries in Cu, NiAl, Al_2O_3, $SrTiO_3$ and ZrO_2 and phase boundaries (metal-ceramic interfaces) in Nb/Al_2O_3, Cu/Al_2O_3 (see the case study in the next section) and Al/$MgAl_2O_4$ [5].

11. Structure and Composition of the Cu/Al_2O_3 Heterointerface

11.1 Film Growth, Orientation Relationship and Structure of Thin Films

Thin films of Cu were grown by molecular beam epitaxy (MBE) on (0001) α-Al_2O_3 substrates [84]. The deposition was carried out at a substrate temperature of 200°C in UHV conditions. A single crystalline 1.1μm thick Cu film was formed on the α-Al_2O_3. Cross-sectional and plan-view TEM investigations confirm the well defined orientation relationship indicated by in situ RHEED streaks, whereby the close-packed planes and close-packed directions between Cu and α-Al_2O_3 are parallel: $(\bar{1}11)$Cu [110]Cu || (0001)Al_2O_3 $[10\bar{1}0]Al_2O_3$.

HRTEM micrographs of the Cu/Al_2O_3 interface edge-on illustrate that both, the close-packed planes and close-packed directions of Cu and Al_2O_3 are parallel to one another. The lattice image shown in Fig. 14 was taken along the [211]Cu and $[2\bar{1}\bar{1}0]Al_2O_3$ zone axes with a high-voltage high-resolution TEM (JEOL-ARM 1250). The $(0\bar{2}2)$ Cu planes with a spacing of 0.128nm are readily visible. The $(\bar{1}11)$ Cu planes and (0006) Al_2O_3 planes are parallel to the interface. The Cu/Al_2O_3 interface is atomically flat and reveals a sharp transition between the α-Al_2O_3 substrate and the copper overgrowth. The interface is devoid of possible reaction phases between Cu and α-Al_2O_3. This is ascribed to the low substrate temperature of 200°C and the UHV conditions used during growth.

The specimen was tilted by 30° in the microscope and the same area was investigated with the [110]Cu and $[10\bar{1}0]Al_2O_3$ directions parallel to the incoming electron eam (Fig. 14b). The same results are obtained as for the first orientation (Fig. 14a).

The epitaxial orientation relationship leads to a mismatch of about 7% between the corresponding spacings of the adjacent Cu and

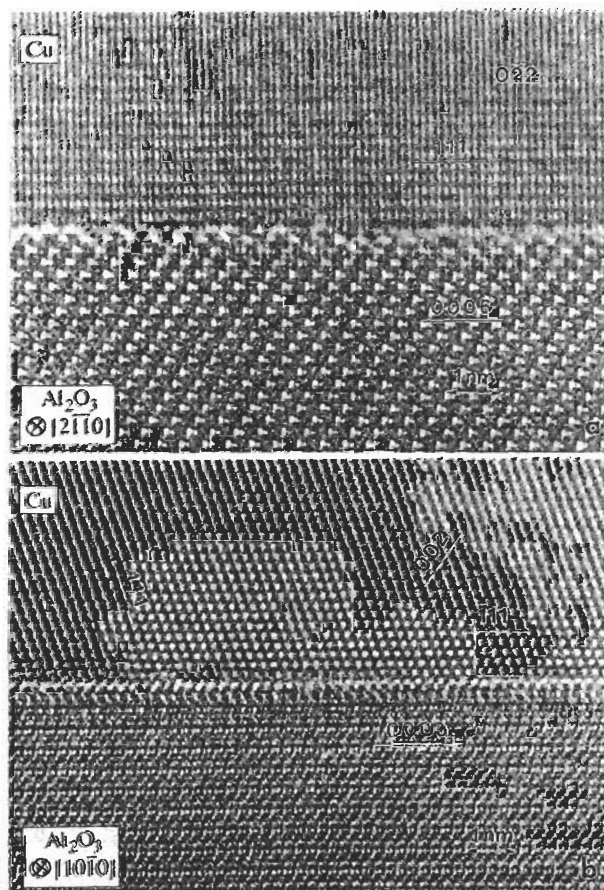

Fig. 14 (a) Lattice image of the atomically flat Cu/α-Al2O3 interface taken along the [211]Cu and $[2\bar{1}\bar{1}0]Al_2O_3$ zone axes reveals no misfit dislocations. The clearly resolved $(0\bar{2}2)$ Cu planes have a spacing of 0.128nm; (b) After tilting the same area of the Cu/α-Al_2O_3 interface into the [110]Cu and $[10\bar{1}0]Al_2O_3$ zone axes the $[\bar{1}11]$Cu, $[\bar{1}\bar{1}1]$Cu and [002]Cu planes can be imaged.

α-Al_2O_3 lattices. In order to minimize the interfacial energy either misfit dislocations can accommodate the lattice disregistry or the two lattices form a strain-free incoherent interface. It was shown that the Cu/Al_2O_3 interface is strainfree and incoherent [67,84].

11.2 Atomic Structure of the Cu/α-Al_2O_3 Interface

The HRTEM investigations described above demonstrate that the interface is atomically flat; thus, the (0001) plane of α-Al_2O_3, which consists of an alternating stacking sequence of oxygen and aluminium layers, could be either terminated by an oxygen or aluminium layer at the interface. Then, either Cu-O bonds or Cu-Al bonds are expected to establish across the Cu/Al_2O_3 interface. The type of bonding can be determined by EELS studies of the fine structure of the Al, O, and Cu ionization edges [14,85]. The ELNES of an ionization edge contains the information about local coordination and electronic structure. Thus, local changes of the oxidation state of Cu at the interface due to bonds with the oxygen sublattice of α-Al_2O_3 or a metallic interface bonding between Cu and the Al-sublattice will modify the ELNES.

The measurements were carried out on the VG HB501 dedicated STEM. The spectra were recorded by applying the spatial difference technique [14,49,50]. The interface was aligned edge-on and spectra recorded in the substrate, in the film and at the interface with the beam scanning an area of $3\times4nm^2$. All spectra were corrected for dark current and read-out pattern of the parallel detector. The pre-edge background was extrapolated by a power law and subtracted from the raw data. The EEL spectrum of the interface was corrected following the method described in ref. [49,50] for both the bulk substrate and film contributions which are present due to the width of the measured area. The remaining difference spectrum represents the ELNES of interfacial atoms possessing a different oxidation state and/or environment compared to the bulk.

The $Al_{L2,3}$ and $Cu_{M2,3}$ edge spectra recorded from the α-Al_2O_3 substrate, the Cu/Al_2O_3 interface and the Cu film lead to a difference spectrum which remains zero within the detection limit. This means that no interface specific component exists within this energy-loss region. Since the $Al_{L2,3}$ ELNES is known to be sensitive to subtle changes in local Al coordination [85], e.g. tetrahedrally and octahedrally coordinated Al in oxides have been distinguished by ELNES studies [14,85], this result indicates that Al does not change its local coordination and so is not involved in bonding at the interface.

In Figure 15 the measured $Cu_{L2,3}$ spectra of the Cu-film (I_{Cu}) and the interface (I_{IF}) are presented. The difference spectrum of the interface (ΔI_{IF}) is shown in Figure 15c. The spectrum was obtained by $\Delta I_{IF} = I_{IF} - aI_{Cu}$, with the scaling factor a = 0.4. Since no electron transitions occur in α-Al_2O_3 within that energy-loss, contributions of bulk α-Al_2O_3 need not be considered. The difference spectrum of the interface reveals a $Cu_{L2,3}$ ELNES which is clearly different from bulk Cu. At an energy-loss of 933eV a L_3 white line is observed for interfacial Cu-atoms. White lines are typical for transition metals and their oxides and arise from electron transitions from 2p-states into empty 3d-states [85]. In metallic Cu^0 all 3d states are occupied and no white line exists in the ELNES (see Fig. 15a), which means, Cu atoms at the interface must possess empty 3d-states. Taking into account that no interface specific component exists for the $Al_{L2,3}$ edge the empty 3d-states in Cu must result from a charge transfer between copper and oxygen at the Cu/Al_2O_3 interface and/or a hybridization of Cu-3d and O-2p states. Comparing the interfacial $Cu_{L2,3}$ ELNES (Fig. 15c) to reference spectra of Cu_2O (nominally Cu^{1+}) and CuO (nominally Cu^{2+}, Fig. 15d,e) indicates that the nominal oxidation state of Cu at the interface is Cu^{1+}, since no chemical shift, which is typical for Cu^{2+}, is detected.

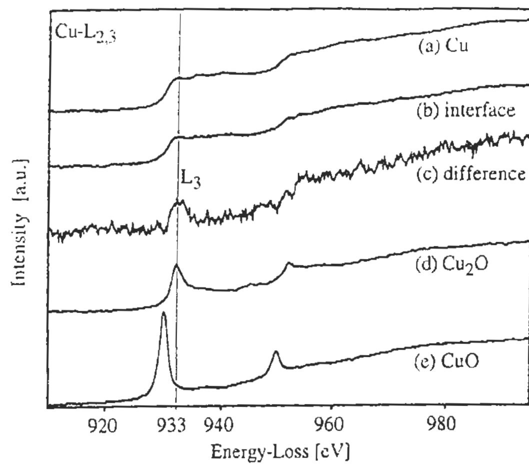

Fig. 15 $Cu_{L2,3}$ ELNES acquired in a region of 3×4 nm2 in (a) the Cu-film and (b) at the Cu/Al_2O_3 interface. The (c) difference spectrum, which contains the interface specific component shows a white line at 933 eV for interfacial Cu atoms due to Cu-O bonds at the interface. Reference spectra of (d) Cu_2O and (e) CuO indicate a nominal Cu^{1+} oxidation state for Cu atoms at the Cu/Al_2O_3 interface.

Examination of the O_K interface difference ELNES indicates that oxygen has changed its local environment at the interface. A direct comparison of the difference spectrum with the bulk α-Al_2O_3 shows a broadening of the main peak at 540eV and a shift to slightly lower energy-losses. At approximately 532eV electron transitions cause a shoulder in the difference spectrum which is not present in bulk α-Al_2O_3. At the same energy-loss a peak is observed in the O_K ELNES of bulk Cu_2O owing to transitions into a hybridized Cu-3d-O-2p state. Furthermore, the peaks above 550 eV change their shape compared to those observed in the O_K ELNES α-Al_2O_3.

The interface specific components found in $Cu_{L2,3}$ and O_K edge imply the presence of ionic-covalent Cu-O bonds across the interface. Image simulations of experimental HRTEM micrographs were then carried out under the assumption of Cu-O bonds at the interface as found by our ELNES studies. A reasonable atomistic model of the interfacial region must result in realistic interatomic spacing across the interface. The best agreement between the experimental and simulated interface image (Fig. 16) was achieved for an average projected bonding distance of 0.2nm ± 0.03nm between the terminating oxygen layer and copper layer. The individual atomic columns fluctuate by the denoted error bar of ±0.03nm around the mean monolayer position. The projected bonding

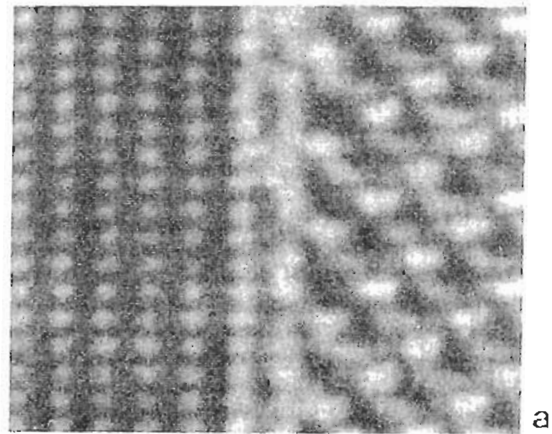

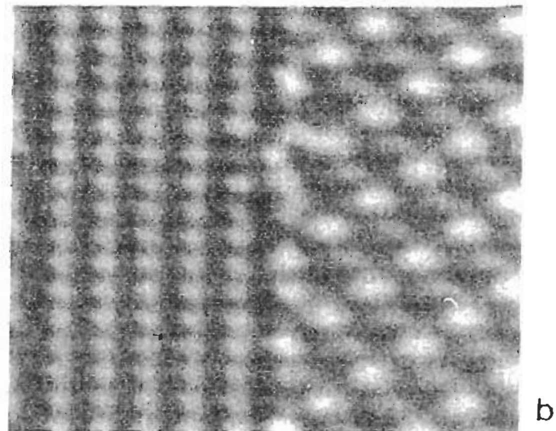

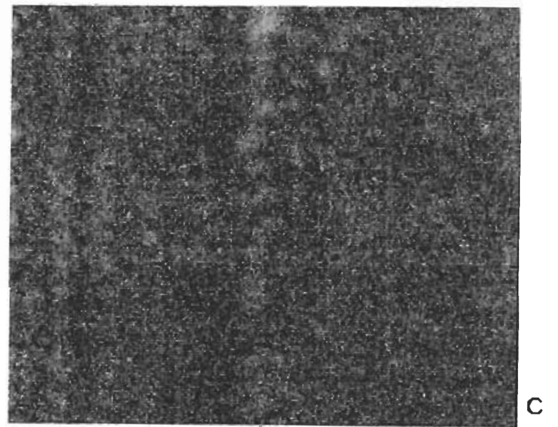

Fig. 16 (a) Experimental and (b) simulated image of Cu/α-Al_2O_3 interface. The positions of the atomic columns are indicated in the simulation. (c) shows the difference image between (a) and (b).

distance of 0.2nm between the terminating oxygen layer and copper layer at the interface appears realistic considering the minimum interatomic spacing in Cu_2O to be 0.18nm. The experimental HRTEM micrograph is presented in Fig. 16a and the corresponding atom positions of the interface model are indicated in the simulated image shown in Fig. 16b.

12. Conclusions

It was shown that different characterization techniques allow the determination of important microstructural parameters of nanomaterials. A broad variety of complementary techniques is available. The different TEM techniques allow the characterization of crystalline materials down to the atomic dimension. This characterization comprises the structure, the chemistry and the bonding on the atomic level. Furthermore, grain misorientation and strains can be determined. In order to gain an optimum in information, constant advancement of the techniques is also required.

The increasing resolution with which structural and compositional information can be obtained also means that the information is extracted from smaller volumes. Hence, a good correlation between macroscopic properties and the underlying structures on an atomistic level can only be obtained for model systems, like planar bimaterial interfaces or layered structures with different components. As an example, we have discussed the results obtained on the Cu/Al_2O_3 interface. We have shown that information can not only be obtained on the local arrangement of the atoms at the interface, but also on the interfacial chemistry and the type of chemical bonding at the interface. The inherent problem of TEM is that for real materials with complex microstructures it may be very critical to infer predictions on macroscopic properties from only a few local areas with nm-size dimensions. Another critical question is as to how much the preparation of the thin TEM specimens may induce artefacts or give non-representative sections through the overall microstructure. Both questions have to be kept in mind in any careful interpretation of TEM results.

Acknowledgement

The author acknowledges interesting and helpful discussions with his colleagues and co-workers at the Max-Planck-Institut für Metallforschung.

References

1. P.B. Hirsch, A. Howie, R.B. Nicholson, D.W. Pashley, M.J. Whelan, Electron Microscopy of Thin Crystals (2nd ed.), Robert E. Krieger Publishing, Huntington, NY 1977.
2. L. Reimer, Transmission Electron Microscopy, Springer, Heidelberg 1994.
3. H. Bethge, J. Heydenreich (edts.), Electron Microscopy in Solid State Physics, Materials Science Monographs, Vol. 40, Elsevier, Amsterdam 1987.
4. D.B. Williams and C.B. Carter, Transmission Electron Microscopy: A Textbook for Materials Science, Plenum Press, New York and London 1996.
5. G. Dehm, F. Ernst, J. Mayer, G. Möbus, H. Müllejans, F. Phillipp, C. Scheu and M. Rühle, Z. Metallkde 87 (1996) 898.
6. J.C.H. Spence, Experimental High-Resolution Electron Microscopy (2nd ed.), Oxford University Press, New York and Oxford 1988.
7. S. Horiuchi, Fundamentals of High-Resolution Transmission Electron Microscopy, Elsevier Science, Amsterdam 1994.
8. J.C.H. Spence and J.M. Zuo, Electron Microdiffraction, Plenum Press, New York 1994.
9. Z.L. Wang, Elastic and Inelastic Scattering in Electron Diffraction and Imaging, Plenum Press, New York and London 1995.
10. D.C. Joy, A.R. Romig, Jr., J.I. Goldstein (edts.), Principles of Analytical Electron Microscopy, Plenum Press, New York 1986.
11. R.F. Egerton, Electron Energy-Loss Spectroscopy in the Electron Microscope (2nd ed.), Plenum Press, New York 1996.
12. M.M. Disko, C.C. Ahn and B. Fultz, Transmission Electron Microscopy in Materials Science, TMS, Warrendale, PA, 1992.
13. L. Reimer (edt.), Energy-Filtering Transmission Electron Microscopy, Springer Series in Optical Sciences Vol. 7, Springer, Berlin, Heidelberg 1995.
14. J. Bruley, Microsc. Microanal. Microsc. 4 (1993) 23.
15. R. Brydson, H. Sauer, W. Engel, J.M. Thomas, E. Zeitler, J. Chem. Soc. Comm. 15 (1989) 1010.
16. D.A. Bonnell (edt.), Scanning Tunnelling Microscopy and Spectroscopy: Theory, Techniques and Applications, VCH Inc., Weinheim 1993.
17. R. Wiesendanger, Scanning Probe Microscopy and Spectroscopy: Methods and Applications, Cambridge University

Press 1994.
18. B. Baretzky, B. Reinsch, U. Täffner, G. Schneider and M. Rühle, Z. Metallkunde 87 (1996) 332.
19. L. Reimer, Scanning Electron Microscopy, Springer, Berlin 1985.
20. P.F. Schmidt, Praxis der Rasterelektronenmikroskopie und Mikrobereichsanalyse, Expert Verlag, Renningen-Malsheim 1994.
21. D.E. Newbury, D.C. Joy, P. Echlin, C.E. Fiori, J.I. Goldstein (edts.), Advanced Scanning Electron Microscopy and X-ray Microanalysis, Plenum Press, New York 1986.
22. J.C. Rivière, Surface Analytical Techniques, Clarendon Press, Oxford 1990.
23. D.J. Dingley, K. Baba-Kishi, Scanning Electron Microscopy, Vol. ii, (1986) pp.383-391.
24. R.A. Schwarzer, Texture and Microstructure 20 (1993) 7.
25. B.L. Adams, S.I. Wright, K. Kunze, Metall. Trans. 24A (1993) 819.
26. B.L. Adams, Materials Science Forum 207-209 (1996) 13.
27. G.F. Van der Voort, Metallography: Principles and Practice, McGraw Hill, New York 1984.
28. G. Pezow, Metallographisches, keramigraphisches, plastographisches Ätzen (6th ed.), Gebrüder Bornträger, Berlin 1994.
29. E.E. Underwood, Quantitative Stereology, Addison-Wesley, Reading, MA, 1970.
30. R. Anderson (edt.), Specimen Preparation Techniques for Transmission Electron Microscopy of Materials II, Mat. Res. Soc. Symp. Proc. 199 (1990).
31. R. Anderson, B. Tracy, J. Bravman (edts.), Specimen Preparation Techniques for Transmission Electron Microscopy of Materials III, Mat. Res. Soc. Symp. Proc. 254 (1992).
32. S.J. Klepeis, R. M. Anderson, R. Anderson, B. Tracy, J. Bravman (edts.), Mat. Res. Soc. Symp. Proc. 115 (1988) 179.
33. U. Salzberger, A. Strecker, J. Mayer, Electron Microscopy 92, Vol. 2 (A. Lopez-Galindo, J. Rodriguez-Garcia, eds.), Granada, Spain (1992) 743.
34. A. Strecker, U. Salzberger, J. Mayer, Prakt. Metallogr. 30 (1993) 481.
35. J. Mayer, Microscopy and Analysis 25 (1993) 21.
36. J. Mayer, D.V. Szabó, M. Rühle, M. Seher and R. Riedel, J. Europ. Ceram Soc. 15 (1995) 717.
37. A. Jalowiecki, J. Bill, F. Aldinger, J. Mayer, Composites Part A, 27A (1996) 717.
38. A. Berger, J. Mayer and H. Kohl, Ultramicroscopy 55 (1994) 101.
39. M. Friess, J. Bill, F. Aldinger, D.V. Szabó, R. Riedel, Key Eng. Mat. 89-91 (1994) 95.
40. S. Lanio, H. Rose and D. Krahl, Optik 73 (1986) 56.
41. J. Bihr, G. Benner, D. Krahl, A. Rilk, E. Weiner, in: Proc. 49th Ann. Meeting EMSA (G.W. Bailey, edt.) San Francisco Press (1991) 354.
42. O.L. Krivanek (edt.), Proc. 2nd Int. Workshop on Electron Energy Loss Spectroscopy and Imaging, Microsc. Microanal. Microstruct. 6 (1995) 1-157.
43. R.F. Egerton, P.A. Crozier, J. Microsc. 148 (1987) 157.
44. O.L. Krivanek, C.C. Ahn, R.B. Keeney, Ultramicroscopy 22 (1987) 103.
45. S.J. Pennycook, D.E. Jesson, Ultramicroscopy 37 (1991) 14.
46. P.E. Batson, Nature 366 (1993) 727.
47. N.C. Browning, M.F. Chisholm, S.J. Pennycook, Nature 366 (1993) 143.
48. J. Bruley, R. Brydson, H. Müllejans, J. Mayer, G. Gutekunst, W. Mader, D. Knauss and M. Rühle, J. Mater. Res. 9 (1994) 2574.
49. H. Müllejans, J. Bruley, Ultramicroscopy 53 (1994) 351.
50. C. Scheu, G. Dehm, H. Müllejans, R. Brydson and M. Rühle, Microsc. Microanal. Microstruct. 6 (1995) 19.
51. J. Marien, Dissertation, Universität Stuttgart (1997).
52. M. Lanham, J. Mayer, S.J. Golden, F.F. Lange, Mat. Res. Soc. Symp. Proc. 169 (1990) 1173.
53. P. Bayle-Guillemand, J. Thibault, Mat. Sci. Forum 207-209 (1996) 197.
54. W. Bollmann, Crystal Defects and Crystalline Interfaces, Springer Verlag, Berlin 1970.
55. J. Greiser, unpublished results.
56. C.J. Schute and J.B. Cohen, J. Mater. Res. 6 (1991) 950; M.R. Doerner and W.D. Nix, J. Mater. Res. 1 (1986) 1.
57. S.K. Streiffer, S. Bader, C. Deininger, J.

Mayer, M. Rühle, Mat. Res. Soc. Symp. Proc. 343 (1994) 615.
58. Y.P. Lin, A.R. Preston and R. Vincent, EMAG 1987, IOP Conference Series No. 90, Institute of Physics, Bristol, p.115.
59. M. Rühle, Microchimica Acta 12 (1992) 75.
[60. H. Müllejans, J. Bruley, J. de Physique IV (1993) 2083.
61. O.L. Krivanek, C. Mory, M. Tencé, C. Colliex, Microsc. Microanal. Microstruct. 2 (1991) 257.
62. H. Müllejans, in: Proc. 1st Slovenian-German Seminar on Joint Projects in Materials Science and Technology (D. Kolar and D. Suvorov, eds.), Jülich GmbH, Jülich (1995) 9.
63. W.D. Kaplan, H. Müllejans, M. Rühle, J. Rödel and N. Claussen, J. Amer. Ceram. Soc. 78 (1995) 2841.
64. R.Brydson, J. Bruley, H. Müllejans, C. Scheu and M. Rühle, Ultramicroscopy 59 (1995) 81.
65. H. Müllejans, R. French, J. Phys. D: Appl. Phys. 29 (1996) 1751.
66. G. Dehm, M. Rühle, H.D. Conway and R. Raj, Acta metall. mater. (1996) in press.
67. G. Dehm, Dissertation, Universität Stuttgart (1995).
68. J. Plitzko and J. Mayer, unpublished results.
69. C. Scheu, unpublished results.
70. M. Op de Beek, D. Van Dyck, W. Cone, Ultramicroscopy 64 (1996) 167.
71. H. Lichte, Ultramicroscopy 64 (1996) 79.
72. A. Tonomura, Electron Holography, Springer Verlag, Berlin 1993.
73. F. Phillipp, R. Höschen, M. Osaki, G. Möbus and M. Rühle, Ultramicroscopy 56 (1994) 1.
74. P. Stadelmann, Ultramicroscopy 21 (1987) 131.
75. D. Hofmann, F. Ernst, Ultramicroscopy 53 (1994) 205.
76. G. Möbus, G. Necker and M. Rühle, Ultramicroscopy 49 (1993) 46.
77. R. Bierwolf, M. Hohenstein, F. Phillipp, O. Brandt, G. Crook, G. Möbus, K. Ploog, Ultramicroscopy 49 (1993) 273.
78. G. Möbus and M. Rühle, Ultramicroscopy 56 (1994) 54.
79. G. Möbus and G. Dehm, Ultramicroscopy 65 (1996) 217.
80. F. Ernst, M.W. Finnis, A. Koch, C. Schmidt, B. Straumal, W. Gust, Z. Metallkde 87 (1996) 911.
81. T. Höche, Dissertation, Universität Stuttgart (1994).
82. G. Möbus, E. Schumann, G. Dehm and M. Rühle, Phys. Stat. Sol. (a) 150 (1995) 77.
83. R. Bierwolf and M. Hohenstein, Ultramicroscopy 56 (1994) 32.
84. G. Dehm, M. Rühle, G. Ding and R. Raj, Phil. Mag. B 71 (1995) 1111.
85. C. Scheu, Dissertation, Universität Stuttgart (1996).